

Electronic Supplementary Information (ESI)

**Gold Nanoparticles decorated carbon nitride nanosheets as
Coreactant Regulate the Conversion of Dual-potential
Electrochemiluminescence of Ru(bpy)₃²⁺ for Hg²⁺ Detection**

Shu-Ping Cao,^a Qiu-Xia Luo,^a Ya-Jie Li,^a Ru-Ping Liang,^{*a} Jian-Ding Qiu ^{*ab}

[†]College of Chemistry, Nanchang University, Nanchang 330031, China

[‡]Engineering Technology Research Center for Environmental Protection Materials
and Equipment of Jiangxi Province, Pingxiang University, Pingxiang 337055, China

*Corresponding authors. Tel/Fax: +86-791-83969518. E-mail: rpliang@ncu.edu.cn; jdqiu@ncu.edu.cn.

EXPERIMENT SECTION

Materials. Dicyandiamide (DCDA), tris(2,2'-bipyridyl) ruthenium(II) hexahydrate powder, hydrogen tetrachloroaurate trihydrate (HAuCl_4), silver nitrate (AgNO_3), chloroplatinic acid (HPtCl_4), palladium chloride (PdCl_2) sodium citrate were obtained from Sigma-Aldrich. Mercuric nitrate ($(\text{HgNO}_3)_2 \cdot \text{H}_2\text{O}$) was acquired from Shanghai precision chemical technology Co. Ltd. Sodium borohydride (NaBH_4), ethanethiol, ascorbic acid (AA), isopropanol were obtained from Sinopharm Chemical Reagent Co. Ltd. Phosphate buffer solution (PBS, 0.1M pH 7.4) containing KH_2PO_4 and K_2HPO_4 in an appropriate ratio with 0.1M KCl was used for ECL detection. All other chemicals were of analytical grade and used as received without further purification. All aqueous solutions were freshly prepared and diluted with ultrapure water ($\geq 18\text{M}\Omega$, Milli-Q, Millipore).

Apparatus. The ECL measurements were performed on a MPI-E multifunctional electrochemiluminescence analyzer (Xi'an Remex Analytical Instrument Ltd. Co., China). The three-electrode ECL cell was consisted of a modified glassy carbon as the working electrode ($\varphi = 3\text{ mm}$), an Ag/AgCl (KCl saturated) electrode as the reference, and a platinum wire as the counter electrode. The photomultiplier tube (PMT) was biased at 800 V, and the scan voltage was from 0 to 1.5 to -1.7 V with the scan rate of 100 mV/s. Ultraviolet-visible light (UV-vis) absorption spectra and fluorescence spectra were obtained with a spectrophotometer (Model UV2450, Shimadzu, Japan) and a spectrophotometer (Model F-7000, Hitachi, Japan), respectively. X-ray photoelectron spectroscopy (XPS) characterizations were measured by a VG Multilab 2000X instrument (Thermal Electron, USA). Fourier transform infrared spectra (FT-IR) were observed on a FT-IR spectrometer (ALPHA, Bruker). Transmission electron microscope (TEM) images were obtained using a JEM-2010 transmission electron microscopy (JEOL, Japan). Cyclic voltammograms (CVs) and electrochemical impedance spectroscopy (EIS) were carried out on an electrochemical workstation (Ivium, Netherlands). CVs were recorded in a potential range between -0.2 V and +0.6 V at a scan rate of 100 mV/s in a solution of 5 mM $\text{K}_3[\text{Fe}(\text{CN})_6]/\text{K}_4[\text{Fe}(\text{CN})_6]$

containing 0.1 M KCl. EIS measurements were performed by applying a voltage of 5 mV amplitude in 0.01 Hz to 10^6 Hz frequency range. Inductively coupled plasma mass spectrometry (ICP-MS, iCAP Q, Thermo Fisher, America) was used to analyze the real samples.

Synthesis of g-C₃N₄ NSs. g-C₃N₄ NSs were prepared following the previously reported literature.¹ Briefly, bulk carbon nitride was prepared by polymerization of DCDA at 500 °C for 4 h under air condition with a ramp of 3 °C·min⁻¹ for the heating processes. Then, the ultrathin g-C₃N₄ NSs were synthesized by exfoliating the as-prepared bulk g-C₃N₄ by liquid exfoliation method. Briefly, 100 mg of bulk g-C₃N₄ powder was dispersed in 100 mL of water and ultrasound was performed for 24 h. The initial formed suspension was then centrifuged to remove the residual unexfoliated carbon nitride. The mass concentration of the g-C₃N₄ NSs suspension was calculated by weighing the powder dried from a certain volume of the suspension.

Preparation of X-g-C₃N₄ NSs (X=Au, Ag, Pt, Pd). X-g-C₃N₄ NSs were prepared according to the literature with a slight modification.² A 10 µL of 0.01 M HAuCl₄ (AgNO₃, HPtCl₄, or PdCl₂) solution was added to 2 mL of the above prepared g-C₃N₄ NSs suspension (*ca.* 2 mg·mL⁻¹) under stirring. The suspension was sonicated for 10 min, followed by a 2 h stirring at room temperature. This process was repeated 3 times. Afterward, 25 µL of 0.01 M freshly prepared NaBH₄ solution was added quickly to the suspension to reduce the AuCl₄⁻, followed by continuously stirring for 20 min. Then, 10 µL of 0.01 M sodium citrate solution was added dropwise into the above suspension, and the stirring was maintained for 30 min. To remove excess NaBH₄, sodium citrate, and unbound nanoparticles, the obtained nanocomposite was separated by centrifugation, washed thoroughly with water, and finally redispersed in 2 mL of ultrapure water for further use and characterization.

Synthesis of Au NPs (cat.5 nm): Au NPs (cat.5 nm) were prepared by the same synthesis process of Au-g-C₃N₄ NSs without g-C₃N₄ NSs as template and then stored at 4 °C.

Synthesis of Au NPs (cat.13 nm): Au NPs (cat.13 nm) were prepared following

the previously reported literature.³ In brief, 24.5 mL H₂O and 0.5 mL 2% HAuCl₄·4H₂O solution was added into a 50 mL round flask, and was heated to boiling. Then, under vigorous whisking, 1 mL of 5% sodium citrate solution was rapidly added. The solution was maintained at the boiling state for 5 min, then cooling the solutions of Au NPs under ambient condition and stored at 4 °C.

Synthesis of Au NPs (cat.30 nm): Au NPs (cat.30 nm) were prepared following the previously reported literature.⁴ In brief, 0.35 mL of 2% HAuCl₄·4H₂O solution was added into a 50 mL round flask, and was heated to boiling. Then, under vigorous whisking, 0.8 mL of 1% sodium citrate solution was rapidly added. The solution was maintained at the boiling state for 15 min, then cooling the solutions of Au NPs under ambient condition and stored at 4 °C.

Synthesis of Au NPs-g-C₃N₄ NSs: A 50 µL of the same concentration of Au NPs solution with three different sizes was added to 2 mL of the above prepared g-C₃N₄ NSs suspension (ca. 2 mg·mL⁻¹) under stirring. The suspension was sonicated for 30 min, followed by a 2 h stirring at room temperature. This process was repeated 3 times. To remove the excess unbound gold nanoparticles, the obtained nanohybrid materials were separated by centrifugation, washed thoroughly with water, and finally redispersed in 2 mL of ultrapure water for further use and characterization.

Fabrication of ECL biosensor. First the glassy carbon electrode (GCE) was polished with 1.0, 0.3, and 0.05 µm α-Al₂O₃ slurry on chamois leather. After ultrasonic cleaning in nitric acid solution, ethanol and ultrapure water for 1 min respectively, the electrode was dry under N₂. Then, 10 µL Au-g-C₃N₄ NSs (0.05 mg mL⁻¹) was dropped on the GCE surface, and dried at room temperature to form Au-g-C₃N₄ NSs/GCE working electrode for further use.

ECL Characterization and Hg²⁺ Detection. The detection of Hg²⁺ on an Au-g-C₃N₄ NSs/GCE electrode was performed in a solution of 100 mM pH 6.0 PBS containing 100 µM Ru(bpy)₃²⁺ at room temperature. Meanwhile, a desire amount Hg²⁺ was added to above-mentioned Ru(bpy)₃²⁺ solution and characterized in a potential range from 0 to +1.5 V to -1.7 V by an ECL technique using 800 V bias.

Characterization of Au-g-C₃N₄ NSs. Nearly transparent g-C₃N₄ NS suspension (Fig. S1) was acquired by the liquid exfoliation method from bulk g-C₃N₄ in water.⁵ Because of the abundant negative charges at the surfaces (Fig. S2), the g-C₃N₄ NSs dispersed in aqueous solution is stably for several months without any sedimentation.



Fig. S1. Photograph of the g-C₃N₄ nanosheets suspension.

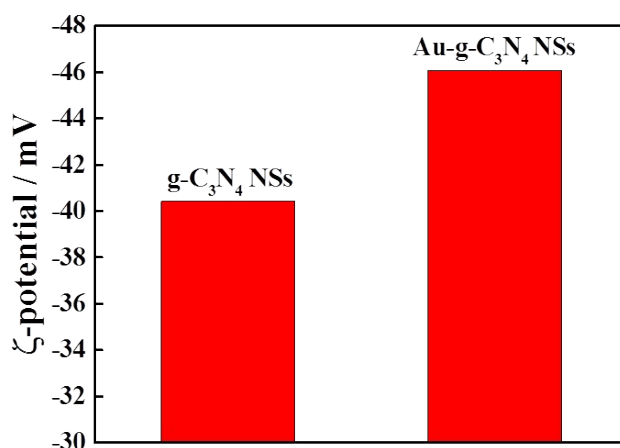


Fig. S2. Zeta potential of the g-C₃N₄ NSs and Au-g-C₃N₄ NSs.

The FT-IR spectroscopy is a powerful tool for analyzing functional groups of g-C₃N₄ NSs. As shown in Fig. S3, a strong peak at 806 cm⁻¹ appears due to the tri-s-triazine ring sextant out-of-plane bending and the intensity of peaks at 1563 and 1246 cm⁻¹ are attributable to the stretching vibrations of C-N(-C)-C and C-NH-C, as well as the peak at 3172 cm⁻¹ is attributed to the N-H stretching vibration and hydrogen-bonding interactions absorption bands.⁶ As for the FT-IR spectra of Au-g-C₃N₄ NSs, the N-H stretching vibration decreases and an additional the Au-N stretching vibration appears at 444 cm⁻¹,⁷ confirming that AuNPs generates on the surface of g-C₃N₄ NSs via Au-N bond.

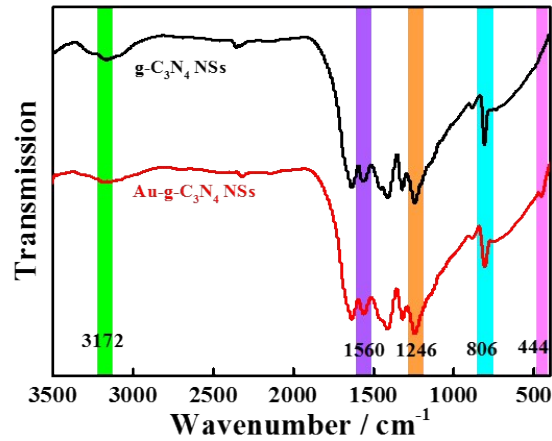


Fig. S3. FT-IR spectra of g-C₃N₄ NSs and Au-g-C₃N₄ NSs.

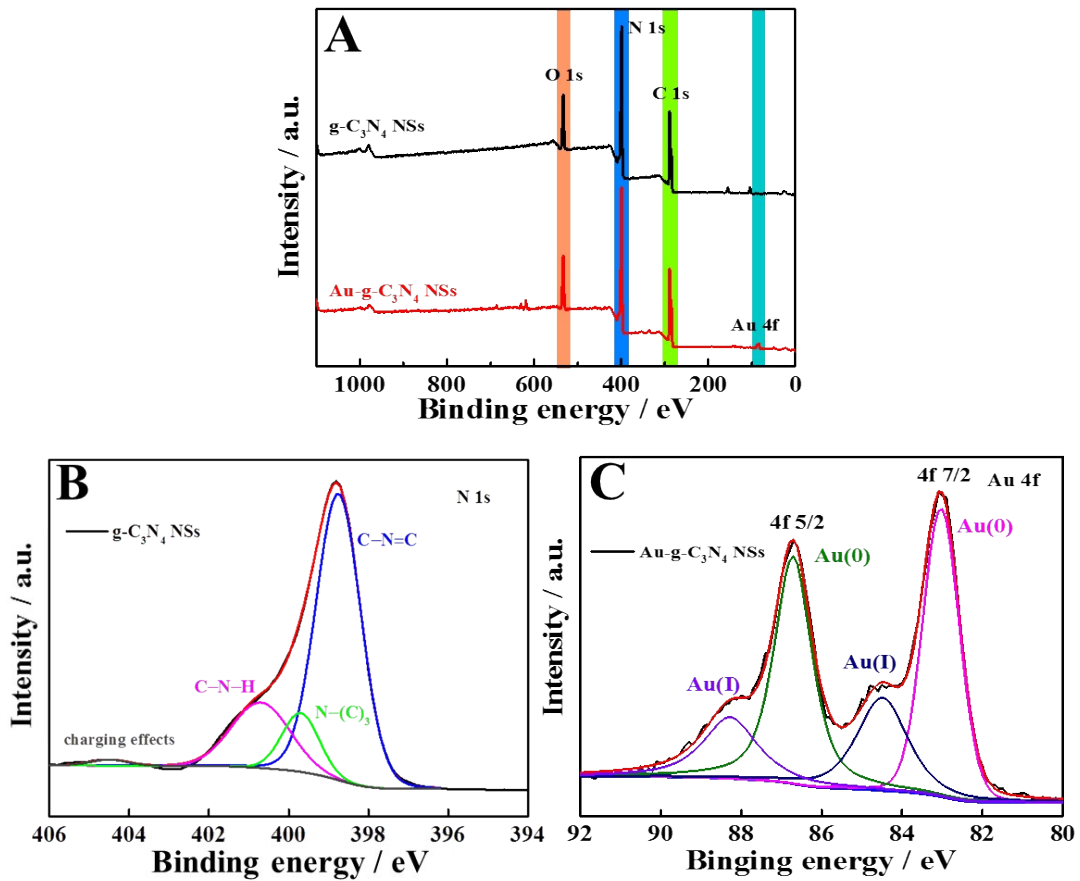


Fig. S4. XPS spectra of (A) g-C₃N₄ NSs and Au-g-C₃N₄ NSs, (B) N 1s peak of g-C₃N₄ NSs, (C) Au 4f region of Au-g-C₃N₄ NSs.

The modulated chemical structure of the g-C₃N₄ NSs and Au-g-C₃N₄ NSs were further confirmed by X-ray photoelectron spectra (XPS). The main elements of

carbon and nitrogen in Fig. S4A, black line and additional element of gold in Fig. S4A, red line demonstrate the successful preparation of g-C₃N₄ NSs and Au-g-C₃N₄ NSs.⁸ The high-resolution N 1s spectrum in Fig. S4B can be deconvoluted into four Gaussian-Lorentzian peaks with the binding energies at 398.6 eV (sp²-bonded nitrogen in N-containing aromatic rings (C–N=C)), 399.7 eV (tertiary nitrogen N–(C)₃ groups), 400.7 eV (amino group (C–N–H)) and 404.2 eV (charging effects or positive charge localization in heterocycles).⁹ This confirms the presence of amino groups on the g-C₃N₄ NSs. In the Au 4f region of Au-g-C₃N₄ NSs (Fig. S4C), the Au 4f_{5/2} at 88.3 V and 4f_{7/2} at 84.5 eV are attributed to Au(I), as well as the Au 4f_{5/2} at 87.2 V and 4f_{7/2} at 83.4 eV are attributed to Au(0).¹⁰ The existence of Au(I) in Au-g-C₃N₄ NSs implies the presence of Au–N bonding interaction.¹¹

The TEM image of g-C₃N₄ NSs shows a two-dimensional sheet-like structure (Fig. S5A). As shown in Fig. S5B, a number of homogeneously and highly dispersed Au NPs are uniformly distributed on the g-C₃N₄ NSs surfaces via the inherent –NH₂– and –NH– functional groups (Fig. S3, S4) which brought about dozens of anchoring sites and facilitated the reduction of AuCl₄[–] on the surface of g-C₃N₄ NSs. The average size of Au NPs is approximately 2 nm. Compared with g-C₃N₄ NSs, Au-g-C₃N₄ NSs display a characteristic absorption peak of spherical Au NPs at 500 nm (Fig. S5C), further confirming the synthesis of Au NPs on the g-C₃N₄ NSs. The XRD patterns (Fig. S5D) were also used to confirm the deposition of Au NPs. The as prepared g-C₃N₄ NSs have a characteristic diffraction peak at 27.2°, which is associated with the (002) interlayer diffraction of graphitic-like structure,¹² also verifying the successful exfoliation of layered g-C₃N₄ NSs. After the deposition of Au NPs, new diffraction peaks at 38.2° and 44.4°, typical peaks for the (111) and (200) planes of Au NPs,² respectively, are observed (curve b in Fig. S5D), indicating the deposition of Au NPs on the g-C₃N₄ NS. The intensity of the (111) peak is much stronger than that of the (200) peak, suggesting that Au (111) plane is the predominant crystal facet in the synthesized Au NPs.

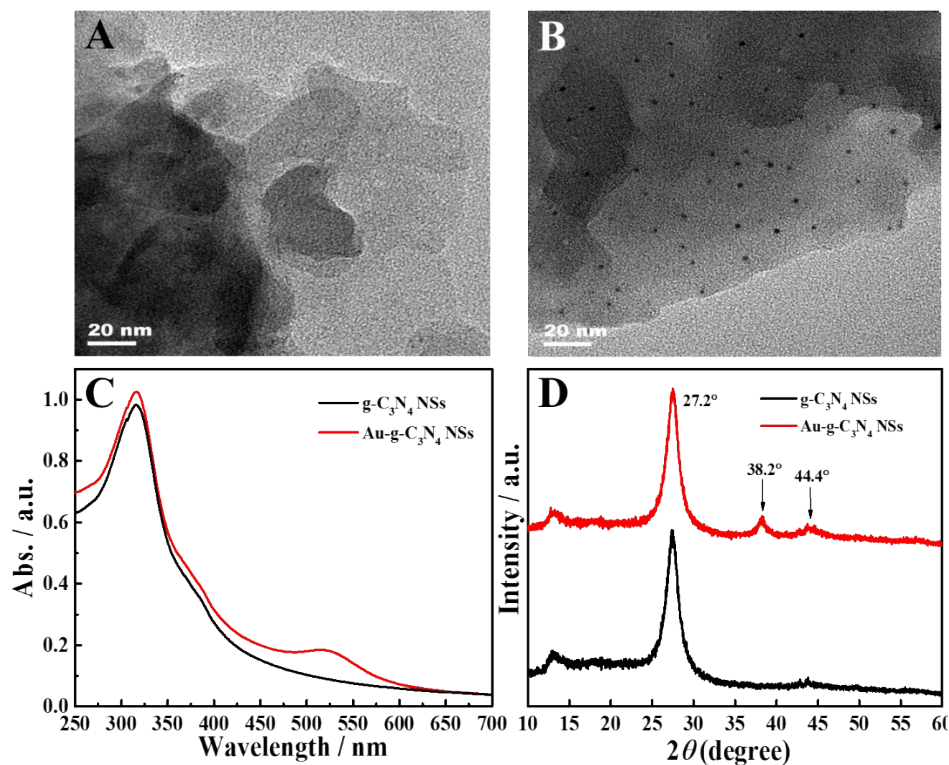


Fig. S5. TEM images of (A) g-C₃N₄ NSs and (B) Au-g-C₃N₄ NSs. (C) UV-vis absorption spectra of g-C₃N₄ NSs and Au-g-C₃N₄ NSs. (D) XRD patterns of g-C₃N₄ NSs and Au-g-C₃N₄ NSs.

Electrochemical Characterization. The preparation of the modified electrodes were confirmed by electrochemical impedance spectroscopy (EIS) and cyclic voltammetry (CV). As shown in Fig. S6A, the bare GCE shows a small semicircle domain (curve a), which illustrates a low electron-transfer resistance (Ret) to the redox couple of [Fe(CN)₆]^{3-/4-}. Compared to the bare GCE, g-C₃N₄ NSs as a semiconductor material dropped on the electrode surface increases the Ret value a little (curve b). Comparatively speaking, the Ret value of Au-g-C₃N₄ NSs/GCE is less than g-C₃N₄ NSs/GCE due to the great electrical conductivity of Au NPs (curve c). As for the cyclic voltammetry in Fig. S6B, it is claimed to correspond to the electrochemical impedance spectroscopy and the results are consistent. All these demonstrate that the ECL platform is fabricated resoundingly.

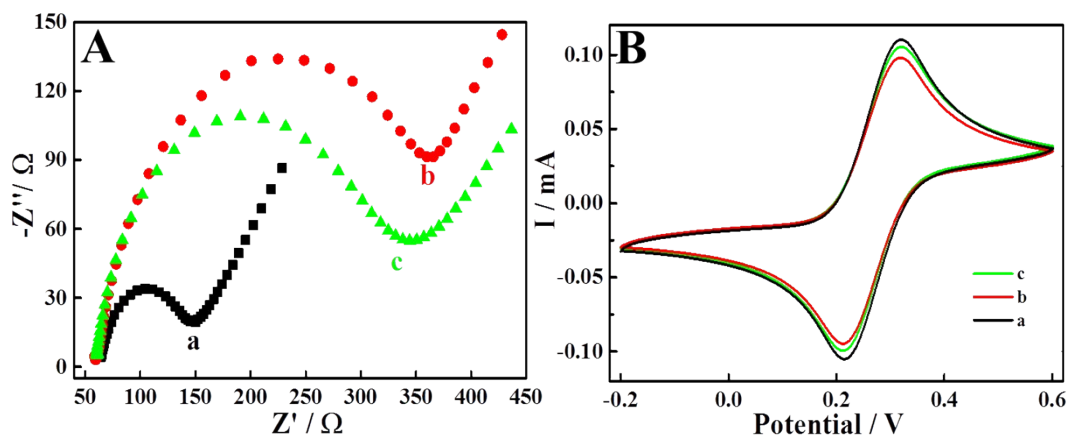


Fig. S6. (A) EIS and (B) CV spectroscopy of bare GCE (a), g-C₃N₄ NSs/GCE (b), Au-g-C₃N₄ NSs/GCE (c).

The ECL spectra were collected to confirm the ECL emitter of this system. In the Au-g-C₃N₄ NSs/GCE-Ru(bpy)₃²⁺ system, an intense cathodic ECL emission peak at 610 nm and a relatively weak cathodic ECL peak at 460 nm are obtained (Fig. S7A), which are consistent with the fluorescence (FL) spectrum of Ru(bpy)₃²⁺ ($\lambda = 610$ nm) (Fig. S7B, curve a) and Au-g-C₃N₄ NSs ($\lambda = 460$ nm) (Fig. S7B, curve b) respectively. Therefore, a small amount of excited state Au-g-C₃N₄ NSs* and a mass of Ru(bpy)₃^{2+*} are generated, and Au-g-C₃N₄ NSs* would ultimately transfer its energy to Ru(bpy)₃^{2+*} based on the overlapped absorption of Ru(bpy)₃²⁺ (Fig. S7B, curve c) and the emission of Au-g-C₃N₄ NSs. At the same time, the anodic ECL is also peaked at 610 nm (Fig. S7C). These results confirm the ECL of Ru(bpy)₃²⁺-Au-g-C₃N₄ NSs/GCE mainly originated from Ru(bpy)₃²⁺, and the intense ECL is attributed to the coreactant effect of Au-g-C₃N₄ NSs. It is the first time reported that Au-g-C₃N₄ NSs can be applied as on-electrode cathodic coreactant of Ru(bpy)₃²⁺.

In the case of g-C₃N₄ NSs/GCE, the anodic ECL emission appears at 610 nm (Fig. S7D), which is also in agreement with the FL spectrum of Ru(bpy)₃²⁺ ($\lambda = 610$ nm) rather than g-C₃N₄ NSs ($\lambda = 460$ nm) (Fig. S7B, curve d), confirming the Ru(bpy)₃²⁺ is indeed the ECL luminophor. For the same reason, energy transfer between the excited state g-C₃N₄ NSs and Ru(bpy)₃²⁺ could also occur due to the spectral overlap.

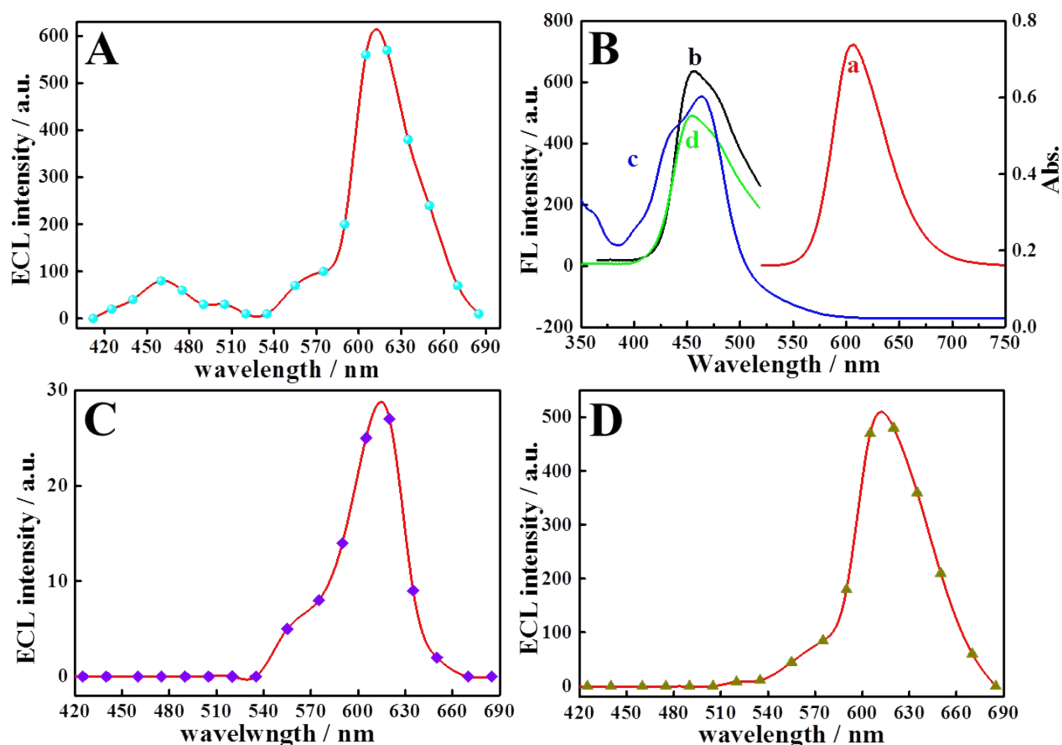


Fig. S7. (A) Cathodic ECL spectra of Au-g-C₃N₄ NSs/GCE-Ru(bpy)₃²⁺ system, PMT=800 V. (B) FL spectra of Ru(bpy)₃²⁺ (a), Au-g-C₃N₄ NSs (b), UV-vis absorption spectra of Ru(bpy)₃²⁺ (c), and FL spectrum of g-C₃N₄ NSs (d). (C) Anodic ECL spectra of Au-g-C₃N₄ NSs/GCE-Ru(bpy)₃²⁺ system, PMT=800 V. (D) Anodic ECL spectra of g-C₃N₄ NSs/GCE-Ru(bpy)₃²⁺ system, PMT=900 V.

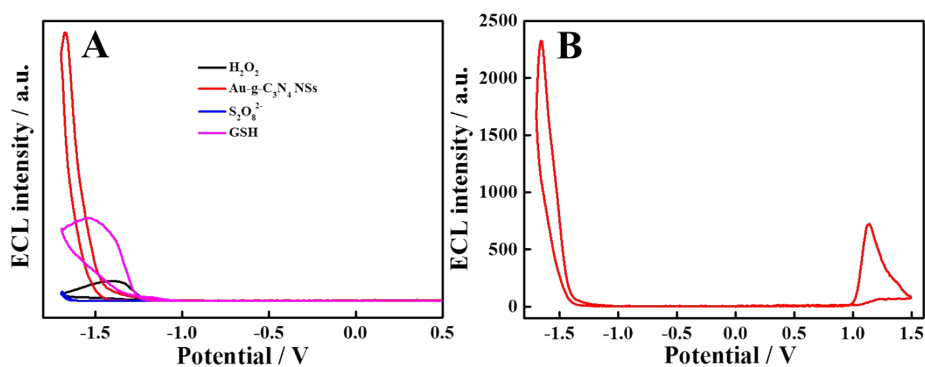


Fig. S8. (A) Responses of 100 μM Ru(bpy)₃²⁺ at the GCEs modified with various coreactants (0.1 mg mL⁻¹) in PBS pH 6 at the scan rate of 0.05 V/s. (B) The ECL signal after Au-g-C₃N₄ NSs is mixed with Ru(bpy)₃²⁺ in solution.

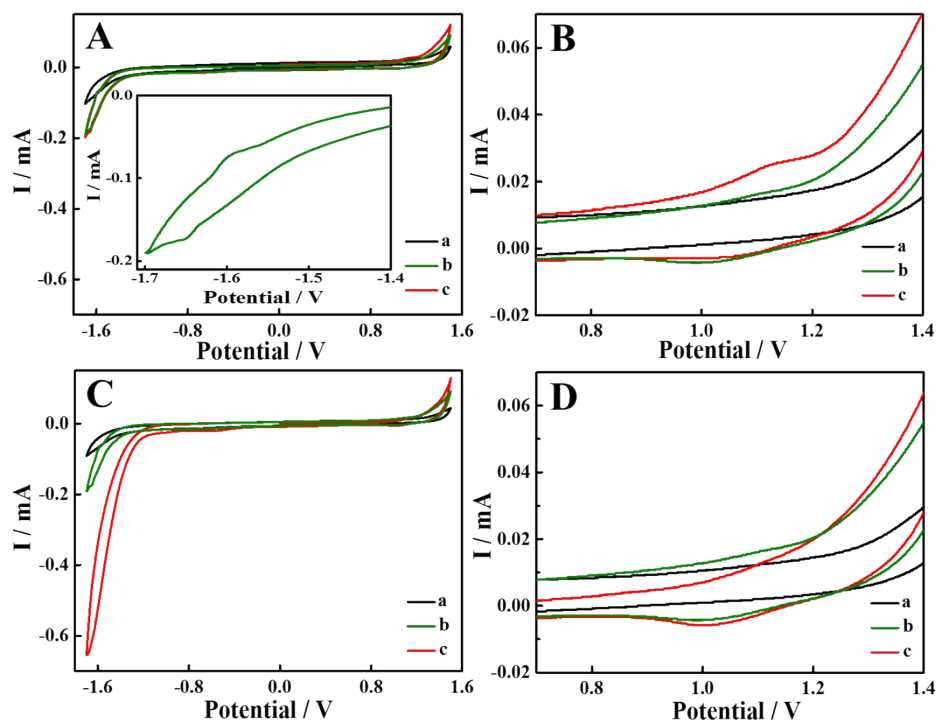


Fig. S9. CV curves of the (A) g-C₃N₄ NSs/GCE in PBS (a), the bare GCE in 100 mM Ru(bpy)₃²⁺ (b) and g-C₃N₄ NSs/GCE in 100 mM Ru(bpy)₃²⁺ (c), insert: the enlarged picture of curve b from -1.4 V to -1.7 V; (B) the enlarged picture of curves in (A) from 0.7 V to 1.4 V; (C) Au-g-C₃N₄ NSs/GCE in PBS (a), bare GCE in 100 mM Ru(bpy)₃²⁺ (b) and Au-g-C₃N₄ NSs/GCE in 100 mM Ru(bpy)₃²⁺ (c); (D) the enlarged picture of the curves in (B) from 0.7 V to 1.4 V.

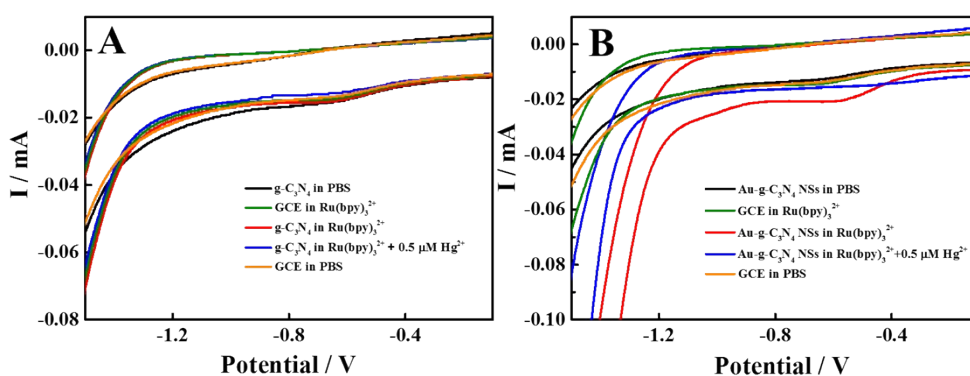
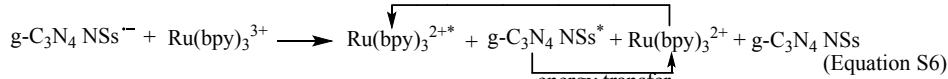
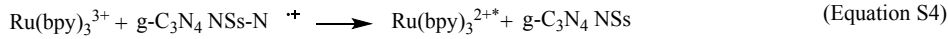
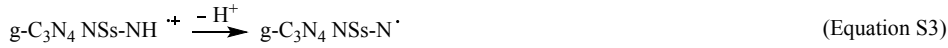


Fig. S10. Enlarged CVs of the (A) g-C₃N₄ NSs/GCE and (B) Au-g-C₃N₄ NSs/GCE in 0.1 M PBS (black lines), 100 μM Ru(bpy)₃²⁺ without (red lines) and with (blue lines) 0.5 μM Hg²⁺; bare GCE in PBS solution (orange lines), 100 μM Ru(bpy)₃²⁺ (green lines).

The mechanisms of anodic Ru(bpy)₃²⁺ ECL at the g-C₃N₄ NSs/GCE. The mechanisms of anodic Ru(bpy)₃²⁺ ECL at the g-C₃N₄ NSs/GCE is similar to the Ru(bpy)₃²⁺-TPA system.¹³ First, Ru(bpy)₃²⁺ loss one electron to generate Ru(bpy)₃³⁺ (Equation S1) and g-C₃N₄ NSs loss one electron and one proton to form g-C₃N₄ NSs-N[•] (Equation S2-S3) at a positive potential. Ru(bpy)₃³⁺ reacts with g-C₃N₄ NSs-N[•] to generate excited state Ru(bpy)₃^{2+*} (Equation S4). In addition, g-C₃N₄ NSs receive one electron to become g-C₃N₄ NSs^{•-} (Equation S5) which then reacts with Ru(bpy)₃³⁺ to gain Ru(bpy)₃^{2+*} (Equation S6) at a negative potential. Ru(bpy)₃^{2+*} releases energy (hv) to generate anodic ECL (Equation S7). A small fraction of the anodic signal and the weak cathodic ECL indeed comes from the Ru(bpy)₃²⁺ annihilation ECL. Hence, the mechanism equations can be described as follows:



The oxidation potential of Au NPs. The peak oxidation potential for the Au NPs ($E_{\text{Au NPs}}$) (the diameter from 0 to 6 nm) was calculated based on the Plieth equation.¹⁴

$$E_{\text{Au NPs}} = \left(-\frac{2\gamma V_m}{ZF} \right) \left(\frac{2}{d} \right) + E_{\text{bulk}} \quad (\text{Equation S8})$$

where E_{bulk} is the oxidation potential of the bulk metal (taken as 0.99 V),¹⁴ γ is the surface tension (1880 erg cm⁻²),¹⁵ V_m is the molar volume (10.21 cm³ mol⁻¹),¹⁵ Z is the number of electrons, F is Faraday's constant, and d is the NP diameter. Therefore, the oxidation potential of Au(0) to Au(I) was calculated to be 0.592 V.

The CV curve of 0.5 mg mL⁻¹ Au-g-C₃N₄ NSs showed no obvious oxidation peak of Au(0) to Au(I) because the low load of AuNPs (Atomic ratio of Au was 0.49% obtained from XPS). When the concentration of Au-g-C₃N₄ NSs was 5 mg mL⁻¹,

compared to g-C₃N₄ NSs, an evident oxidation peak of AuNPs (Au(0) to Au(I)) appeared at 0.6 V (Fig. S11) which was consistent with the theoretical calculation.

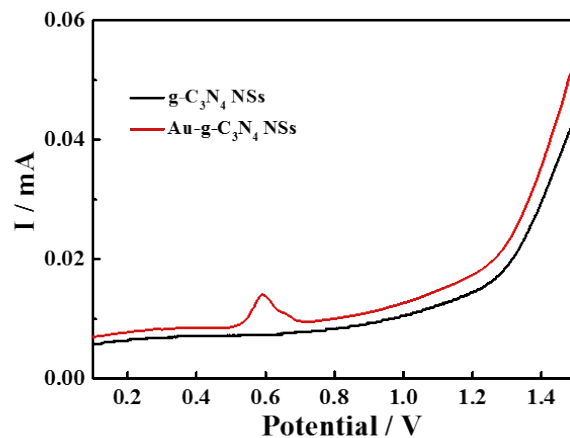


Fig. S11. DPV curves of 5 mg mL⁻¹ g-C₃N₄ NSs (black curve) and 5 mg mL⁻¹ Au-g-C₃N₄ NSs (red curve) in PBS solution.

Regulation of AuNPs under Different Conditions. While rotating different concentrations of ethanethiol on Au-g-C₃N₄ NSs, the cathodic ECL intensities gradually decreased but the anodic ECL didn't change (Fig. S12B). This can be explained by that the formation of the Au-S bond annihilated the activity of the AuNPs. In situ synthesis of AuNPs generally disallowed tailoring their size and morphology.² Thus, the size effect was studied by using pre-synthesized different size AuNPs of 5 nm, 13 nm and 30 nm. Different sizes of AuNPs with same concentration were attached to the g-C₃N₄ NSs respectively (Fig. S13). The cathodic signals gradually weakened, and the anodic signals basically remained unchanged with the increase of particle size (Fig. S12C). It means that catalytic activity of AuNPs had a vital influence on the cathodic ECL attributable to the decreased catalytic activity with the augment of particle size. Different nanoparticle-functionalized g-C₃N₄ NSs (X-g-C₃N₄ NSs, X=Ag, Pt, Pd) synthesized in the same way and their effects were studied (Fig. S12D). All the X-g-C₃N₄ NSs can work as a cathodic coreactant, and the enhancement order is Au-g-C₃N₄ NSs > Ag-g-C₃N₄ NSs > Pt-g-C₃N₄ NSs > Pd-g-C₃N₄ NSs, which may be related to the catalytic ability of different nanoparticles.^{16,17}

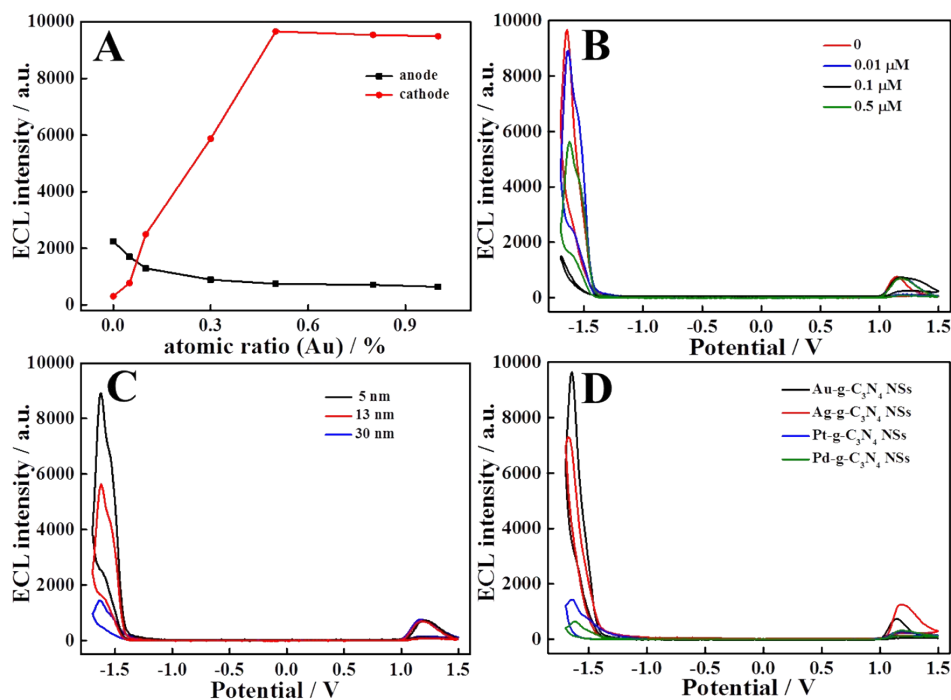


Fig. S12. (A) The effect of atomic ratio of Au on g-C₃N₄ NSs. (B) ECL changes of different concentration of ethanethiol on Au-g-C₃N₄ NSs. (C) ECL intensities at AuNPs (5 nm)-g-C₃N₄ NSs/GCE, AuNPs (13 nm)-g-C₃N₄ NSs/GCE and AuNPs (30 nm)-g-C₃N₄ NSs/GCE. (D) ECL responses of X-g-C₃N₄ NSs/GCE (X=Au, Ag, Pt, Pd). All the detection solution is 100 μM Ru(bpy)₃²⁺ in PBS (0.1 M, pH 6). PMT: 800 V, potential scan rate: 100 mV s⁻¹.

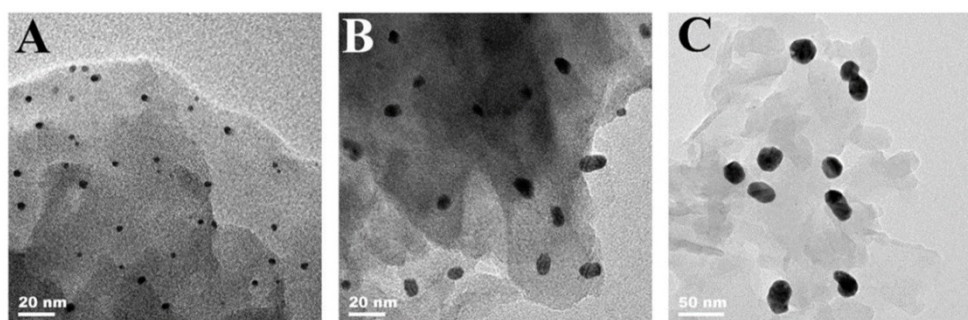


Fig. S13. TEM images of (A) Au NPs (5 nm)-g-C₃N₄ NSs, (B) Au NPs (13 nm)-g-C₃N₄ NSs and (C) Au NPs (30 nm)-g-C₃N₄ NSs.

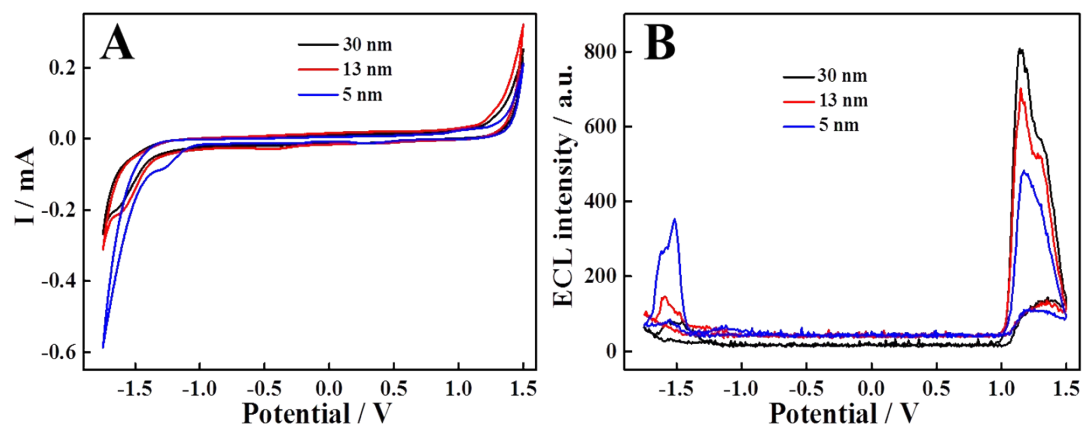


Fig. S14. ECL responses and CVs of the Au NPs (5 nm, 13 nm, 30 nm)/GCE in 100 μM $\text{Ru}(\text{bpy})_3^{2+}$.

Table S1. The XPS atomic of N and Au on Au-g- C_3N_4 NSs synthesized at different concentrations of HAuCl_4

HAuCl_4 Concentrations (mM)	Atomic of total N (%)	Atomic of N(C-N-H) (%)	Atomic of Au (%)
0	42.78	1.31	0
2	43.14	1.22	0.08
5	42.82	1.18	0.18
8	42.86	1.10	0.31
10	42.78	1.02	0.49
12	41.52	0.86	0.60
15	41.62	0.76	0.88

Atomic of N (C-N-H) is the ratio of nitrogen atoms in the amino group to the total number of atoms.

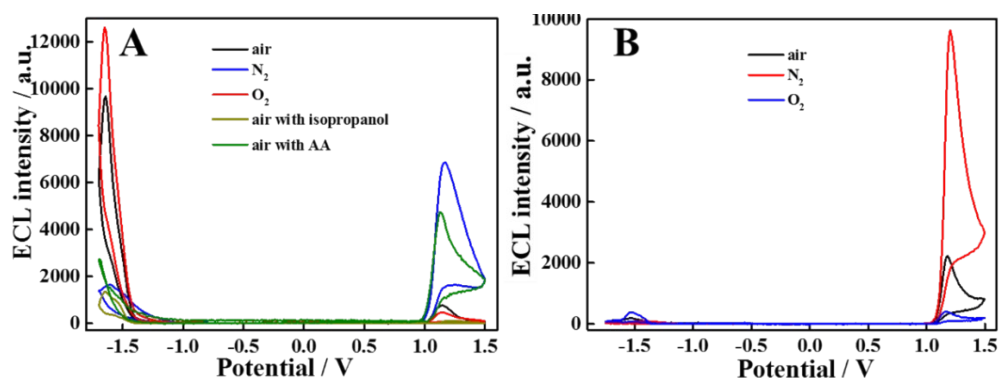


Fig. S15. (A) ECL responses of the Au-g- C_3N_4 NSs/GCE in 100 μM $\text{Ru}(\text{bpy})_3^{2+}$ saturated with air, N_2 or oxygen, and 0.05 mM TEOA saturated with air. (B) ECL

responses of the g-C₃N₄ NSs/GCE in 0.1 M PBS containing 100 μM Ru(bpy)₃²⁺ saturated with argon, air or oxygen.

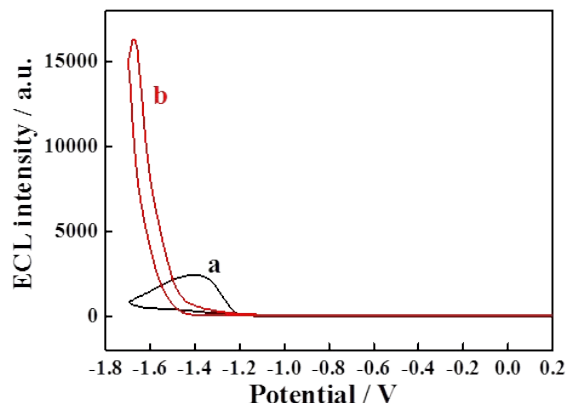


Fig. S16. ECL responses of the bare GCE (a) and Au-g-C₃N₄ NSs/GCE (b) in 100 μM Ru(bpy)₃²⁺ with 500 mM H₂O₂.

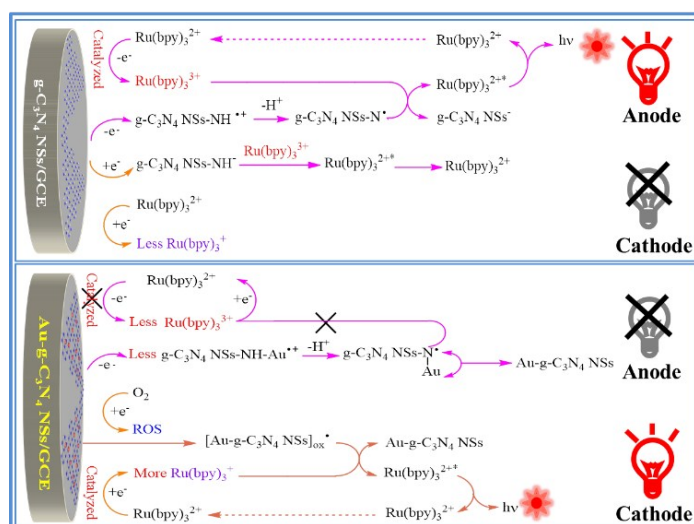


Fig. S17. Different coreactant mechanisms of Au-g-C₃N₄ NSs and g-C₃N₄ NSs with Ru(bpy)₃²⁺.

Calculation of E₁^o [Au-g-C₃N₄ NSs]ox^o/ Au-g-C₃N₄ NSs versus Ag/AgCl.

According to The Nernst equation,¹⁸

$$E_1^o \text{ vs Ag/AgCl} = E_1^o \text{ vs SHE} - \varphi_{\text{Ag/AgCl}}^o \text{ vs SHE} - (RT/zF) \text{ pH} \quad (\text{S9})$$

Thereinto, E₁^o of [Au-g-C₃N₄ NSs]ox^o/ Au-g-C₃N₄ NSs is 1.57 V vs SHE.¹⁹ $\varphi_{\text{Ag/AgCl}}^o$ vs SHE is equal to 0.22V,²⁰ R is the standard gas constant; F is the Faraday constant; T is the thermodynamic temperature; z is the number of electrons in the reaction. The pH of the system is 6. So, E₁^o [Au-g-C₃N₄ NSs]ox^o/ Au-g-C₃N₄ NSs vs Ag/AgCl is calculated to be 0.995 eV

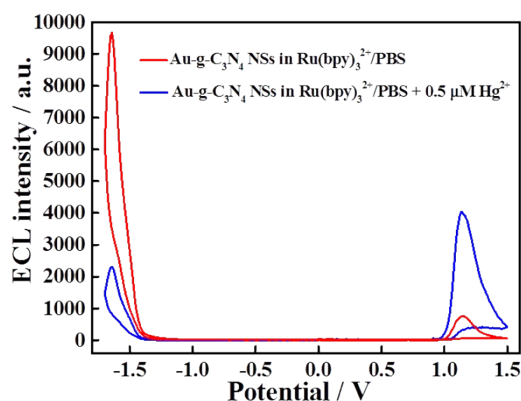


Fig. S18. ECL curves of the Au-g-C₃N₄ NSs/GCE in 100 μM Ru(bpy)₃²⁺ with and without 0.5 μM Hg²⁺.

Optimization of Detection Conditions. To make the ratiometric ECL system of Hg²⁺ detection have optimal and efficient performance, several experimental parameters were optimized, including the detection pH of PBS solution, the concentration of Au-g-C₃N₄ NSs and the concentration of Ru(bpy)₃²⁺. The ratio ECL of anode to cathode ($E_{\text{anode}}/E_{\text{cathode}}$) of Au-g-C₃N₄ NSs/GCE-Ru(bpy)₃²⁺ system without 0.5 μM Hg²⁺ is low at pH ≤ 6 due to the strong cathodic ECL and weak anodic ECL of the system. The $E_{\text{anode}}/E_{\text{cathode}}$ increases when 0.5 μM Hg²⁺ is added because the enhanced anodic ECL and decreased cathodic ECL of the system, and the maximum enhancement is at pH 6. Therefore, the detection pH is chosen at 6.0 on the basis of best signal-to-noise (Fig. S19A). In the coreactant pathway, the best concentrations of luminophor and coreactant are found to be 100 μM (Fig. S19B) and 0.5 mg mL⁻¹ (Fig. S19C), respectively.

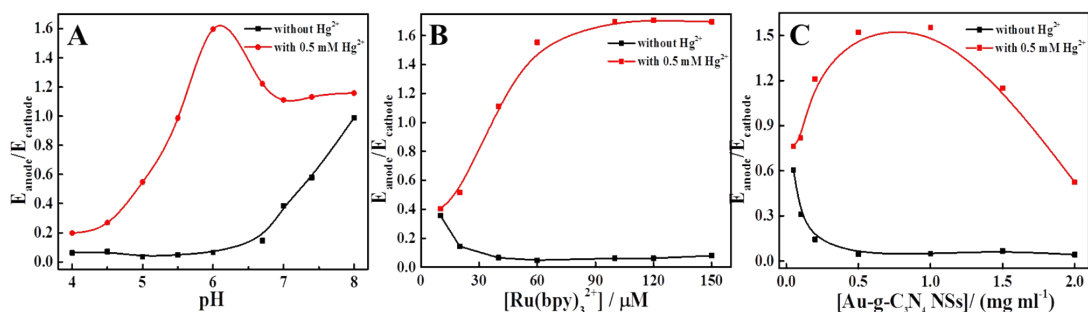


Fig. S19. Effect of (A) detection pH, (B) different concentration of Ru(bpy)₃²⁺ and (C) Au-g-C₃N₄ NSs.

Stability and Reproducibility of the ECL Sensor. The ECL emission of Au-g-C₃N₄/GCE in Ru(bpy)₃²⁺ and the ECL emission from the Au-g-C₃N₄/GCE-Ru(bpy)₃²⁺ system upon addition of 50 nM Hg²⁺ were recorded under continuous potential scanning for eight cycles. The results in Fig. S20 indicated the good stability of the Au-g-C₃N₄/GCE and the proposed sensor for Hg²⁺ detection. The long-time stability of the sensor was investigated. When the sensor was stored at 4 °C, it retained 91.9% of its initial response after a storage period of 2 weeks, indicating the proposed sensor has good long-term stability. The reproducibility of the ratiometric ECL sensor was examined on the same and on the different electrodes with the same Hg²⁺ concentration. Relative standard deviation of five dependent measurements is less than 4.3% for the same electrode and less than 7.6% for five electrodes. Therefore, the ECL platform has a relatively good reproduction in Hg²⁺ detection.

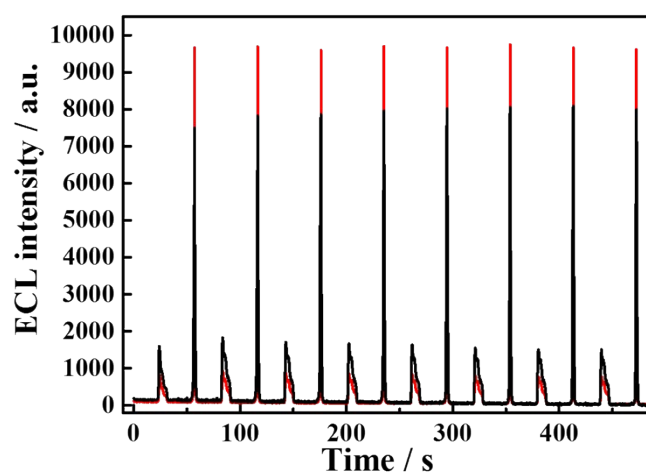


Fig. S20. Stability of ECL emission of Au-g-C₃N₄ NSs/GCE in Ru(bpy)₃²⁺ (red line) and the ECL emission of the sensor for detection of 50 nM Hg²⁺ (black line).

Table S2. Comparison of the different platforms for the detection of Hg²⁺.

Ampl Materials	Detection method	Linear range	LOD	Ref.
Graphene-Rhodamine	Colorimetric Assay	0-1000 nM	2 ppb	21
Gold nanoparticles	Colorimetric Assay	5-40 nM	3 nM	22
N-Hydroxysulfos-uccinimide	Electrochemiluminescence	0.1 -25 μ M	10 nM	23
Gold-Silver Bimetallic Nanoclusters	Electrochemiluminescence	10 nM-5 μ M	5 nM	24
Graphene oxide	Fluorescent	0-1.0 nM	0.3 nM	25
Iridium Complex	Fluorescent	0.2-1.0 μ M	67 nM	26
Gold nanoclusters	Fluorescent	50 nM to 500 μ M	30 nM	27
Exonuclease III	Electrochemical	5 nM to 1020 nM	0.5 nM	28
Nanoporous gold	Electrochemical	0.01-100 nM	3.6 fM	29
Au-g-C ₃ N ₄ /Ru(bpy) ₃ ²⁺	Electrochemiluminescence	0.5-500 nM	0.2 nM	This work

Single-signal Detection of Hg²⁺. Under the same conditions with Ru(bpy)₃²⁺-Au-g-C₃N₄ NSs/GCE system, as shown in Fig. S21A, with increasing the concentration of Hg²⁺, the ECL signal of Ru(bpy)₃²⁺ at the anode increases and a linear relationship ($ECL_{\text{anode}} = 3.58 C_{\text{Hg}^{2+}} + 2059.43$) within the concentration range of 50 nM to 500 nM is observed as shown in Fig. S21B. In the meantime, the limit of detection (LOD) is estimated to be 20 nM (S/N = 3) without any separation and enrichment. This LOD is higher than the limitation in drinking water (2 ppb, ~10 nM) stipulated by EPA. The specificity of this ECL sensor was evaluated by introducing different interfering species into the ECL system. As shown in Fig. S21C, Cu²⁺ can also lead to an obvious decrease in the ECL intensity. This can be attributed to the electron transfer from g-C₃N₄ NSs to Cu²⁺. The stability of the ECL sensor like to the Ru(bpy)₃²⁺-TPA system always needs dozen scanning to get balance (Fig. S21D).

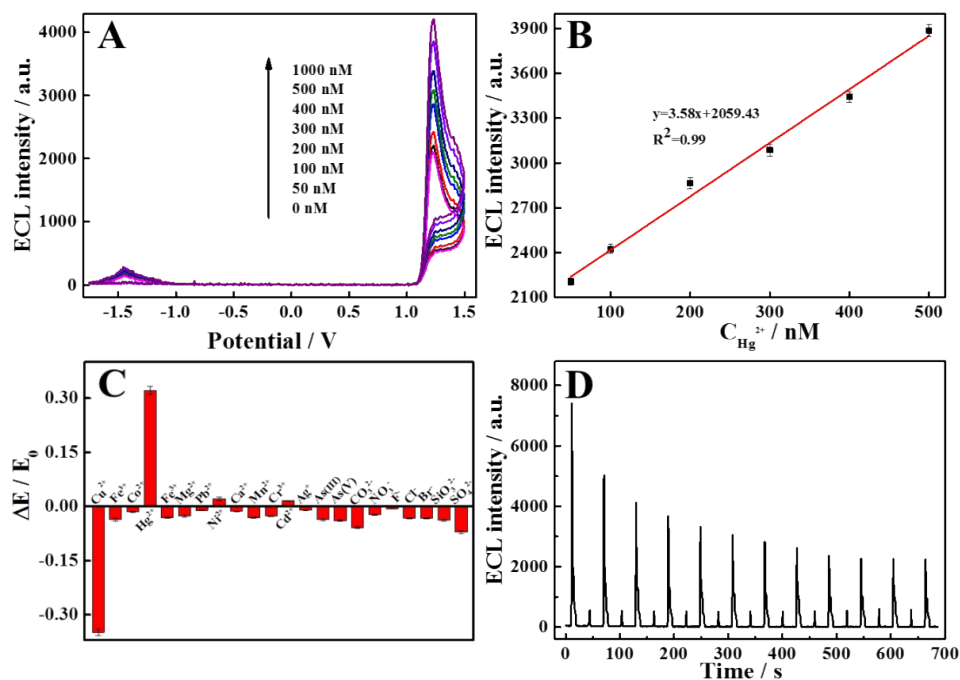


Fig. S21. (A) ECL intensity of sensor with different concentrations of Hg^{2+} (0, 50, 100, 200, 300, 400, 500, 1000 nM); (B) linear relationship between anodic ECL intensity and the concentration of Hg^{2+} in the range of 50–500 nM. (C) Selectivity of the ECL sensor after treatment of 0.1 μM Hg^{2+} , compared with 1 μM of other interference metal ions. (D) Stability of ECL emission of the ECL sensor for the detection of 50 nM Hg^{2+} .

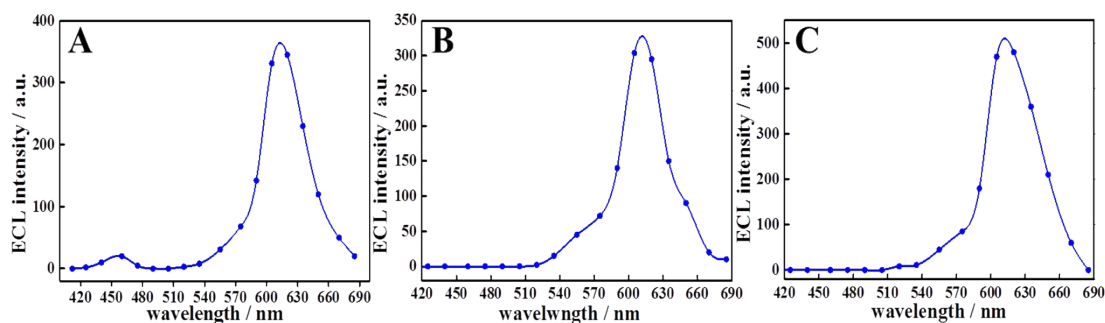
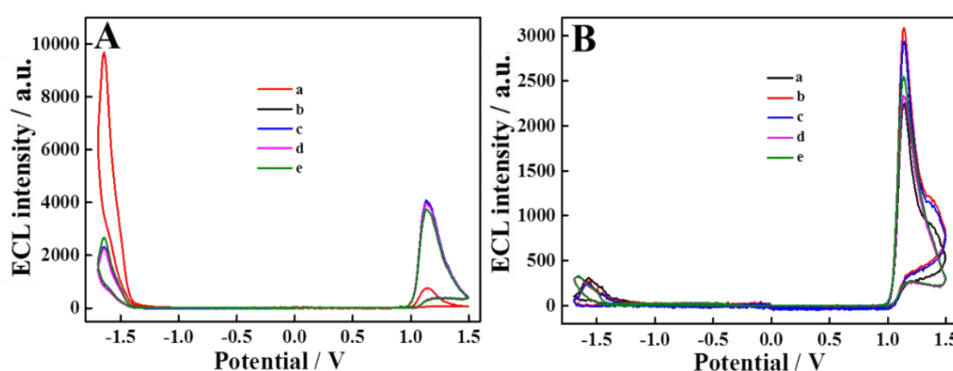
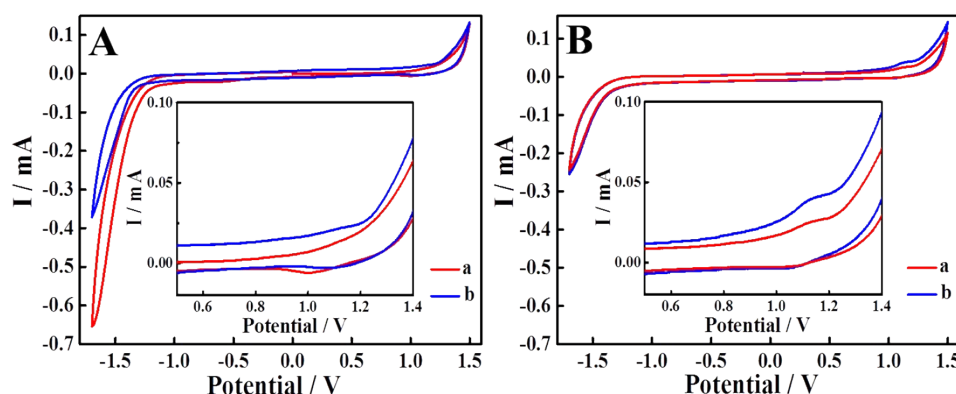


Fig. S22. (A) Cathodic ECL spectra of Au-g- C_3N_4 NSs/GCE- $\text{Ru}(\text{bpy})_3^{2+}$ system with 0.5 μM Hg^{2+} , PMT=800 V; (B) Anodic ECL spectra of Au-g- C_3N_4 NSs/GCE- $\text{Ru}(\text{bpy})_3^{2+}$ system with 0.5 μM Hg^{2+} , PMT=800 V; (C) ECL spectra of g- C_3N_4 NSs/GCE- $\text{Ru}(\text{bpy})_3^{2+}$ system with 0.5 μM Hg^{2+} , PMT=900 V.

Table S3. Hg²⁺ determination in real water samples (n= 3).

Real Sample	Hg ²⁺ added (nM)	Hg ²⁺ detected (nM)	RSD (%)	Recovery (%)
Tap water 1	1	1.05 ± 0.06	5.7	105
Tap water 2	10	9.69 ± 0.58	6.0	96.9
Tap water 3	100	106.50 ± 4.68	4.4	106.5
Lake water 1	1	1.10 ± 0.08	7.3	110
Lake water 2	10	9.80 ± 0.75	7.3	98
Lake water 3	100	96.22 ± 4.53	4.7	96.22
River water 1	1	0.97 ± 0.07	7.2	97.3
River water 2	10	10.84 ± 0.64	5.9	108.4
River water 3	100	108.8 ± 3.37	3.1	108.8

**Fig. S23.** ECL response of (A) Au-g-C₃N₄ NSs/GCE and (B) g-C₃N₄ NSs/GCE in Ru(bpy)₃²⁺ without 0.5 μM Hg²⁺ (a); with 0.5 μM Hg²⁺ (b); with 0.5 μM Hg²⁺ and 0.1 μM EDTA (c); 0.5 μM Hg²⁺ and 0.5 μM EDTA (d); 0.5 μM Hg²⁺ and 5 μM EDTA (e).**Fig S24.** CV curves of the (A) Au-g-C₃N₄ NSs/GCE and (B) g-C₃N₄ NSs/GCE in 100 μM Ru(bpy)₃²⁺ without (a) and with (b) Hg²⁺; Insert: the enlarged CV curves of (A) and (B) in the potential range from 0.5 V to 1.4 V respectively.

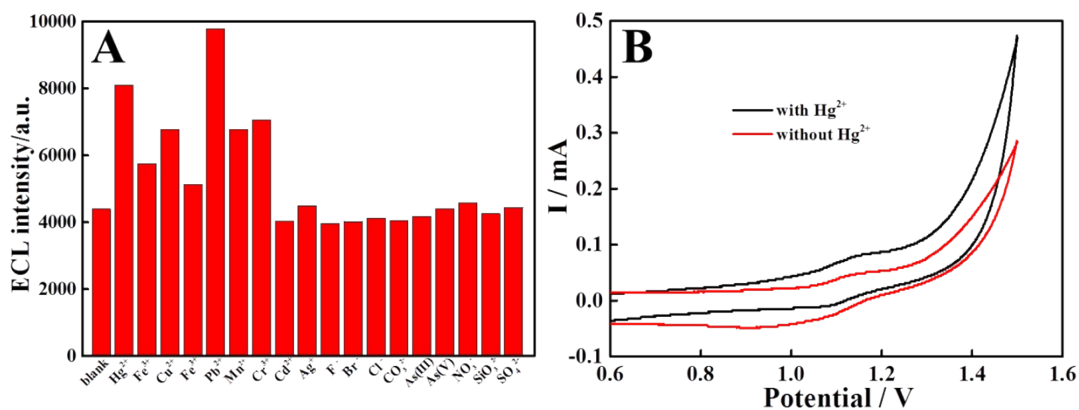


Fig. S25. (A) ECL responses of Ru(bpy)₃²⁺-TPA system in 0.5 μM different ions, (B) CV responses of Ru(bpy)₃²⁺-TPA system without or with 0.5 μM Hg²⁺.

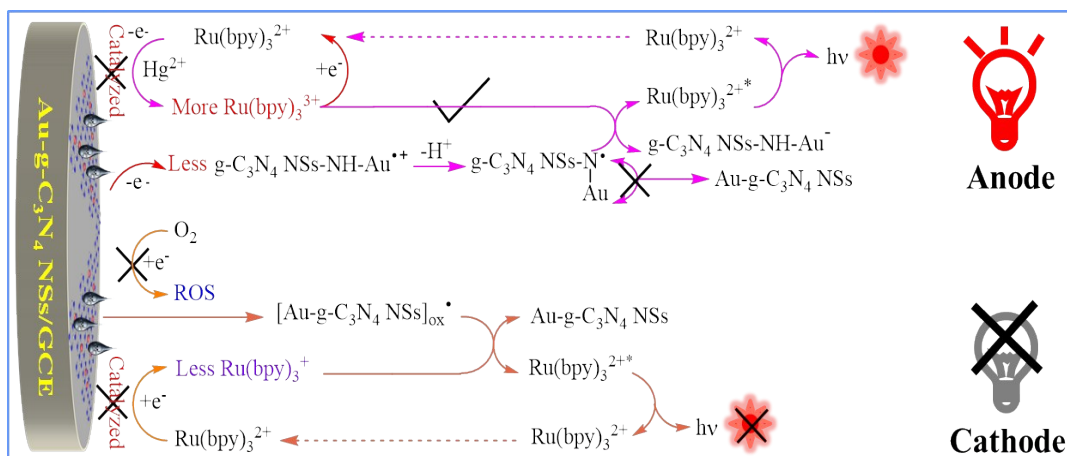


Fig. S26. The ECL mechanism of ratiometric detection Hg²⁺.

Reference

- Q. M. Feng, Y. Z. Shen, M. X. Li, Z. L. Zhang, W. Zhao, J. J. Xu and H. Y. Chen, *Anal. Chem.*, 2016, **88**, 937-944.
- L. Chen, X. Zeng, P. Si, Y. Chen, Y. Chi, D. H. Kim and G. Chen, *Anal. Chem.*, 2014, **86**, 4188-4195.
- J.-Q. Chen, L.-D. Yu, L. Zhang, R.-P. Liang, S.-P. Cao and J.-D. Qiu, *J. Electroanal. Chem.*, 2019, **833**, 449-453.
- H. Jung, J. Jung, Y.-H. Kim, D. Kwon, B.-G. Kim, H. B. Na and H. H. Lee, *BioChip Journal*, 2018, **12**, 249-256.
- J. Ji, J. Wen, Y. Shen, Y. Lv, Y. Chen, S. Liu, H. Ma and Y. Zhang, *J. Am. Chem. Soc.*, 2017, **139**, 11698-11701.
- Y. Z. Wang, N. Hao, Q. M. Feng, H. W. Shi, J. J. Xu and H. Y. Chen, *Biosens. Bioelectron.*, 2016, **77**, 76-82.
- G. Gencheva, D. Tsekova, G. Gochev, D. Mehandjiev and P. R. Bontchev, *Inorg. Chem. Commun.*, 2003, **6**, 325-328.

8. R. P. Liang, L. D. Yu, Y. J. Tong, S. H. Wen, S. P. Cao and J. D. Qiu, *Chem. Commun.*, 2018, **54**, 14001-14004.
9. Z. Zhou, Q. Shang, Y. Shen, L. Zhang, Y. Zhang, Y. Lv, Y. Li, S. Liu and Y. Zhang, *Anal. Chem.*, 2016, **88**, 6004-6010.
10. K. Juodkazis, *Electrochem. Commun.*, 2000, **2**, 503-507.
11. L. Liu, H. Su, F. Tang, X. Zhao and Q. Liu, *Nano Energy*, 2018, **46**, 110-116.
12. L. Tian, P. Zhao, J. Wei, Y. Chi, S. F. Zhou and L. Chen, *ChemElectroChem*, 2019, **6**, 1673-1677.
13. W. Miao, J.-P. Choi and A. J. Bard, *J. Am. Chem. Soc.*, 2002, **124**, 14478-14485.
14. R. A. Masitas and F. P. Zamborini, *J. Am. Chem. Soc.*, 2012, **134**, 5014-5017.
15. W. J. Plieth, *J. Phy. Chem.*, 1982, **86**, 3166-3170.
16. S. K. Das, T. Parandhaman, N. Pentela, A. K. M. Maidul Islam, A. B. Mandal and M. Mukherjee, *J. Phys. Chem. C*, 2014, **118**, 24623-24632.
17. Y. M. Long, L. Bao, J. Y. Zhao, Z. L. Zhang and D. W. Pang, *Anal. Chem.*, 2014, **86**, 7224-7228.
18. M. M. Walczak, D. A. Dryer, D. D. Jacobson, M. G. Foss and N. T. Flynn, *J. Chem. Educ.*, 1997, **74**, 1195.
19. L. Ge, C. Han, J. Liu and Y. Li, *Appl. Cat. A: General*, 2011, **409**, 215-222.
20. L. Angnes, C. M. N. Azevedo, K. Araki and H. E. Toma, *Anal. Chim. Acta*, 1996, **329**, 91-95.
21. A. Mohan and R. Neeroli Kizhakayil, *ACS appl. mater. Interfaces*, 2016, **8**, 14125-14132.
22. L. Tan, Z. Chen, C. Zhang, X. Wei, T. Lou and Y. Zhao, *Small*, 2017, **13**.
23. M. Saqib, S. Bashir, H. Li, C. Li, S. Wang and Y. Jin, *Anal. Chem.*, 2019, **91**, 12517-12524.
24. Q. Zhai, H. Xing, X. Zhang, J. Li and E. Wang, *Anal. Chem.*, 2017, **89**, 7788-7794.
25. J. Huang, X. Gao, J. Jia, J. K. Kim and Z. Li, *Anal. Chem.*, 2014, **86**, 3209-3215.
26. Z. Yang, C. Huang, C. Wang, Y. Zhao and Q. Song, *ACS Sustainable Chem. Eng.*, 2017, **5**, 4443-4448.
27. J. Zang, C. Li, K. Zhou, H. Dong, B. Chen, F. Wang and G. Zhao, *Anal. Chem.*, 2016, **88**, 10275-10283.
28. F. Tan, L. Cong, N. M. Saucedo, J. Gao, X. Li and A. Mulchandani, *J. Hazard. Mater.*, 2016, **320**, 226-233.
29. F. Gao, N. Gao, A. Nishitani and H. Tanaka, *J. Electroanal. Chem.*, 2016, **775**, 212-218.